TUDelft

Delft University of Technology

Autonomous Navigation Performance of Cislunar Orbits considering High Crosslink Measurement Errors

Turan, E.; Speretta, S.; Gill, E.K.A.

Important note
To cite this publication, please use the final published version (if applicable).
Please check the document version above.

Autonomous Navigation Performance of Cislunar Orbits considering High Crosslink Measurement Errors

Erdem Turan, Stefano Speretta, Eberhard Gill
Department of Space Engineering
Delft University of Technology
Kluyverweg 1, 2629 HS Delft
e.turan@tudelft.nl

Abstract—This study investigates the application of the Linked Autonomous Interplanetary Satellite Orbit Navigation (LiAISON) technique for multiple small spacecraft in cislunar orbits considering high inter-satellite range measurement errors. The LiAISON method provides an autonomous orbit determination solution using crosslink measurements such as range, and/or range-rate. Inter-satellite ranging can be done via conventional tone or code based methods. Considering the limited on-board transmission power available on small satellites, ranging and data transfer, required to cope with the limited contact time, introduce further observable degradation and limiting performance. For such cases, and to increase the supported data rates, telemetry ranging and time-derived ranging architectures can be used. Unfortunately, in time-derived methods, measurements are not as accurate as using other methods, limiting the applicability of such technique only to few missions. This paper presents a simulation based analysis to understand the limits of LiAISON for a multi-spacecraft mission at the Earth-Moon L_1, L_2 Halo and Lunar orbits considering high inter-satellite measurements errors due to time-derived and telemetry-based ranging methods and without Doppler measurements. This is specifically targeted at small satellites with limited power budgets and radio links lacking coherent Doppler tracking. The simulation results show that the LiAISON-based autonomous orbit determination works well for configurations of cislunar orbits, having the link between Lagrangian and Lunar orbits, even with high crosslink ranging errors.

TABLE OF CONTENTS

1. INTRODUCTION

In recent years, there has been a growing interest in small satellite missions to the Moon. A significant interest can be observed for the cislunar vicinity due to piggyback opportunities [1]. All those small satellite missions have planned to use traditional ground-based navigation techniques. However, ground-based tracking could be expensive while the development of small satellites shall be at small cost. In addition, it is difficult to track all these small satellites due to limited capacity of ground stations and there are limitations of the small satellite itself such as the power available on-board for communication. Considering all these challenges,

an autonomous navigation architecture for cislunar missions could be a possible solution.

Up to now, there have been various studies on autonomous navigation architectures for deep space and cislunar missions [2–11]. In one of these studies, the Linked Autonomous Interplanetary Satellite Orbit Navigation (LiAISON) method has been proposed [5]. This is an orbit determination technique which uses satellite-to-satellite observations, such as range and/or range-rate, to estimate the absolute states of spacecraft when at least one of them is in an orbit with an unique size, shape, and orientation [5]. The characteristics of the acceleration function are the main factor to decide whether inter-satellite range or range-rate measurements can be used alone to estimate the absolute spacecraft states. In a symmetrical gravitational field, there is no unique orbit resulting from the acceleration function, having also symmetric time derivative, leading to no absolute position determination. Cis-lunar and deep-space missions could benefit from this asymmetric or unique gravity field: for cislunar missions, for example, Hill [4] has shown the effectiveness of the LiAISON method considering orbiters for lunar and Lagragian orbits. Hesar [6] has further investigated LiAISON by adding surface assets on lunar farside and collected observations between the Earth-Moon L_2 (EML$_2$) halo orbit and surface assets. Recently, Wang [7] has shown the LiAISON performance for spacecraft at distant retrograte orbits, Earth orbits and lunar-orbits considering dynamic and clock model errors, demonstrating the LiAISON algorithm capabilities. In the coming period, the Cislunar Autonomous Positioning System Technology Operations and Navigation Experiment (CAPSTONE) mission will test this navigation architecture based on the inter-satellite radiometric data between the CAPSTONE spacecraft and Lunar Reconnaissance Orbiter (LRO) [12].

This approach could reduce ground-based tracking requirements and thus mission cost. The orbit determination performance of this technique depend on various factors, such as the inter-satellite measurement accuracy. It was mentioned in [10] that uncertainties in the force model and measurement noise can counteract the effect of asymmetric perturbations and make the crosslink tracking based orbit determination unfeasible. Up to now, studies have considered accurate inter-satellite ranging with a measurement error typically below $3\,\mathrm{m}$, and coherent Doppler tracking. However, a problem arises for small satellites with limited on-board transmission power available: ranging and data transfer, required to cope with the limited contact time, introduces further observable degradation limiting performance. Basically, if the small satellite requires ranging for its navigation, the ranging signal reduces the power available for telemetry, which reduces the data rate that can be supported [13]. For such cases, and to increase the supported data rates, telemetry-based ranging and time-derived ranging architectures (based on time transfer and time delay measurements) were proposed

in literature [13–17]. Unfortunately, in time-derived methods, measurements are not as accurate as traditional methods, limiting the applicability of such technique only to few specific missions. Current waveforms used for coherent Doppler tracking together with data transmission introduce further modulation losses and require linear amplifiers, further reducing the overall link efficiency and making it unfeasible in many practical cases.

The objective of this paper is to present a simulation-based analysis to understand the limits of LiAISON in the cislunar environment considering high inter-satellite measurement errors. Section 2 presents a brief summary of inter-satellite ranging while Section 3 provides a summary of the dynamical model used. Then, orbit determination models are introduced in Section 4, also detailing observability equations and filtering models. Section 5 presents the simulation results and analysis. Conclusions are drawn in Section 6.

2. INTER-SATELLITE RANGING

In the conventional two-way ranging used by ground stations, an uplink signal (which could be a sequence of discrete tones or a pseudo-noise sequence) is received and re-transmitted by the satellite and received at the ground station to allow the computation of the two-way propagation time. This process can be either regenerative, in which the spacecraft demodulates and acquires the ranging code by correlation with a local replica from the uplink ranging signal and regenerates the ranging code on the downlink, or can be transparent, in which the spacecraft translates the uplink ranging signal to the downlink without code acquisition [18]. These techniques provide different performance as regenerative ranging also allows to correct for communication errors between the ground station and the satellite, actually lowering the required transmitted signal power. These conventional ranging techniques are also applicable for the purpose of inter-satellite ranging (Shown in Figure 1).

Small satellites often lack radio links with coherent Doppler tracking (deep space small satellites can be considered exceptions to this, such as [19, 20]) and could only use two-way non-coherent ranging for navigation. However, using non-coherent pseudo-noise ranging introduces a range bias in the measurements due to a chip rate mismatch between the received code and the local replica [18]. Applying this type of ranging to a deep space satellite formation, composed of a mother and a daughter spacecraft, leads to the following ranging error [18] (considering a pseudo-noise square-wave shaped ranging signal, a chip tracking loop and a wider on-board loop bandwidth for the mothercraft)

$$\sigma_{\rho PN} = \frac{1}{\sqrt{2}} \frac{c}{4 f_{rc}} \sqrt{\frac{B_L}{(P_{RC}/N_0)}} \qquad (1)$$

And the range bias due to a chip rate mismatch

$$\rho_{\text{bias}} = \frac{c \Delta f_{chip} T}{4 f_{chip}} \qquad (2)$$

with c the speed of light, f_{rc} the frequency of the ranging clock component, B_L one-sided loop noise bandwidth, P_{RC} power of the ranging clock component, T integration time,

N_0 one-side noise power spectral density, Δf_{chip} the difference in frequency between the received chip rate and the local chip rate.

Using conventional tone or pseudo-noise ranging, a certain power is required for a downlink ranging signal, which limits the power available for telemetry. On the other hand, telemetry-based ranging provides a round-trip light time solution derived from the telemetry stream [14, 17]. Basically, this method does not require a downlink ranging signal but it provides, as part of the telemetry stream, the delay between acquired ranging signal and start of the next telemetry frame. In the end, all timing data provide a round-trip light time solution on the ground or at the signal source which includes the two-way light time propagation and the re-transmission delay. This method has several advantages: at first, ranging and telemetry can be done at the same time, removing the need to plan tracking and telemetry sessions at different time intervals or multiplexing them; secondly, even low data rates provide a ranging solution as good as that of conventional tone or pseudo-noise ranging. Considering a direct-to-Earth link, telemetry-based ranging provides better than conventional pseudo-noise ranging measurements at a data rate of about 15 kbps while using a correlator [17]. Assuming the speed of light is greater than relative velocity, $v \ll c$, a square wave uplink range clock and BPSK-modulated data, performance of the telemetry-based ranging can be given as [17]

$$\sigma_{\rho TM} = \frac{4 c T_{sd}^2}{\pi T_l E_S/N_0} + \frac{c}{8 f_{rc}} \sqrt{\frac{B_L}{(P_{RC}/N_0)}} \qquad (3)$$

with T_{sd} the channel symbol duration, T_l the correlator integration time and E_S/N_0 the code symbol-to-noise ratio.

In the telemetry-based ranging, the uplink ranging signal is yet required [14] and any type of traditional ranging signal could be used for the uplink side. For this purpose, a more power-efficient solution (instead of the most accurate) could be selected considering the case for a small satellite implementing a cross-link.

Another way to compute the round-trip light time between satellites is based on time transfer, as in the CCSDS Proximity-1 Space Link Protocol [21] where time correction, correlation and distribution are standard services. Users can exchange epochs between satellites and derive the round-trip light time using dedicated algorithms to deal with physical limitations. A basic explanation of this process is given in Figure 2 [22]: t_1 is the S/C-A timestamp at the time of transmission to S/C-B, while t_2 is the reception timestamp on S/C-B. Similarly, t_3 and t_4 are the S/C-A and S/C-B timestamps at the time of transmission and reception respectively. When each S/C obtains the four successive timestamps, the round trip light time and offset can be calculated [22]. Here, the change in position of both spacecraft during the signal round trip projected along the line-of-sight direction and the overall clock bias are neglected.

For Spacecraft A,

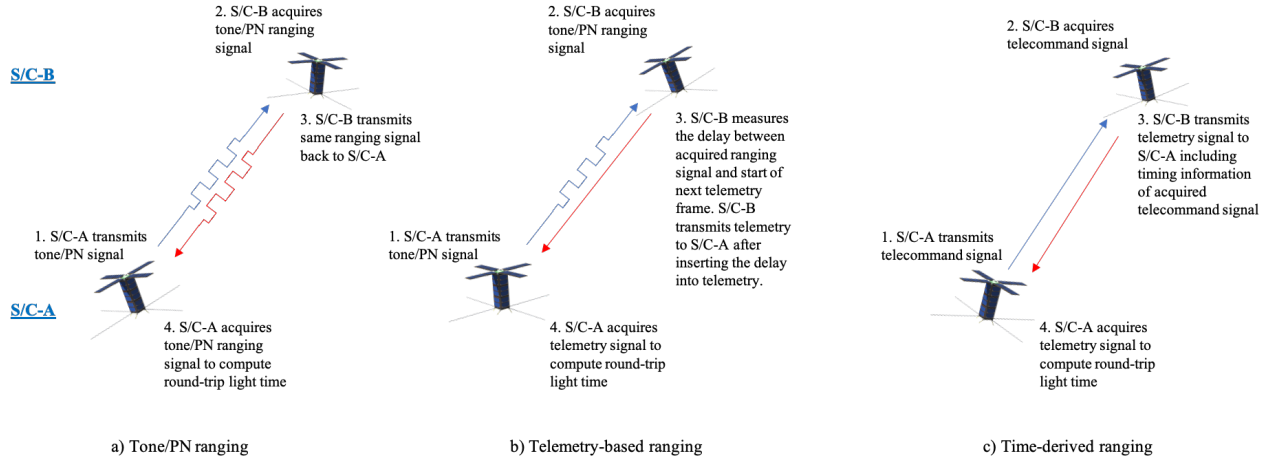$$\text{Offset} = \frac{1}{2} \{[t_2 - t_1] + [t_3 - t_4]\}$$

2

Figure 1. Ranging methods, [17, 18], for crosslink purposes. Arrows containing square shapes represent Tone/PN ranging signal while straight arrows represent telecommand/telemetry signal only.

$$\text{RTLT Delay} = [t_4 - t_1] - [t_3 - t_2]$$

For Spacecraft B,

$$\text{Offset} = \frac{1}{2}\left\{[t_4 - t_3] + [t_5 - t_6]\right\}$$

$$\text{RTLT Delay} = [t_6 - t_3] - [t_5 - t_4]$$

In [15], a very similar method was proposed, where the round-trip light time has been measured from ping requests directly using the satellite radio. From the hardware testing, a ranging accuracy has been found as $155\,\mathrm{m}\,(1\sigma)$ under strong signal conditions and $303\,\mathrm{m}\,(1\sigma)$ under realistic worst-case conditions for $10\,\mathrm{kbps}$ data rate. Strong signal conditions refer to a Bit Error Rate (BER) 10^{-5} or lower while worst case conditions refer to a BER of 10^{-4}. Basically, this method does not provide an accurate ranging solution, but this can still be sufficient to meet navigation requirements for certain missions. If timing is measured in units of telemetry/telecommand symbols, instead of directly in seconds, the downlink equation given in Equation 3 of the telemetry-based ranging could be used for both link sides. Based on the same assumptions used in Equation 3, and assuming T_l, E_S/N_0 are the same on both downlink and uplink sides, the performance of the time-derived ranging is
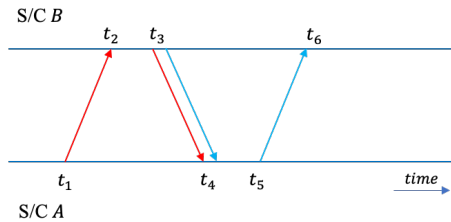

Figure 2. Representation of the round-trip light time calculation [22].

$$\sigma_{\rho_{TD}} = \frac{4\,c\,\sqrt{T_{sd\,U}^4 + T_{sd\,D}^4}}{\pi\,T_l\,E_S/N_0} \tag{4}$$

with $T_{sd\,U}$ and $T_{sd\,D}$ the symbol duration for uplink and downlink respectively.

Comparison of these three ranging methods is shown in Figure 3. As it can be seen, the conventional pseudo-noise ranging is not a function of data-rate. On the other hand, telemetry-based ranging and time-derived ranging method show improved performance with increased data rate.
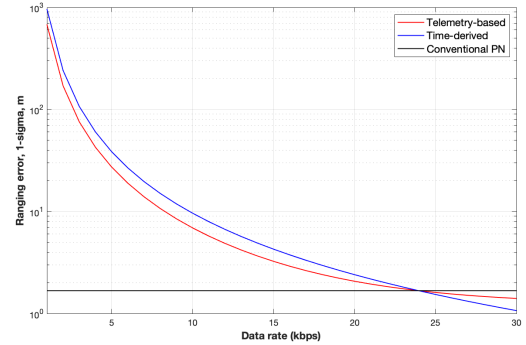
Figure 3. Performance comparison of the ranging methods.

The aim of this study is to focus on high measurement errors (as can be the case for small satellite missions with constrained hardware) and time-derived ranging method is considered for the rest of this study.

3. DYNAMICAL MODEL

The dynamic models in this study are formulated as Circular Restricted Three-body Problem (CRTBP). This assumes that two primary bodies, the Earth and the Moon in this case, are moving on circular orbits around their mutual barycenter. This model is simple but accurate enough for many theoretical and practical applications such as [23]. In [5],

3

Figure 4. Diagram of the Circular Restricted Three-Body Problem with a rotating, nondimensional coordinate frame.

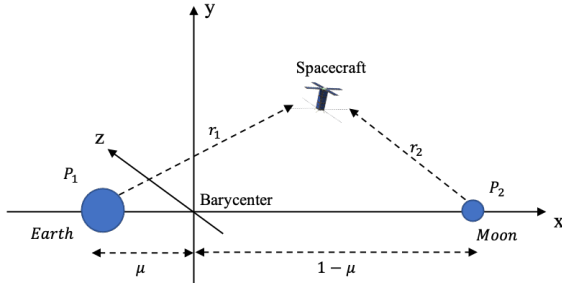the orbit determination accuracy is compared for various force models (CRTBP and JPL DE405 Ephemeris) for the autonomous Lagrange point orbiter missions. It is found that the orbit determination accuracy remained in the same order of magnitude, so that the CRTBP is selected for the analysis in this study.

Considering two massive bodies, P_1 and P_2 moving under the action of their mutual gravitation, and their orbit around each other be a circle of radius r_{12}. As shown in Figure 4, a non-inertial, co-moving frame of reference is defined whose origin lies at the barycenter of the two-body system. The positive x direction goes from P_1 to P_2. The positive y axis is parallel to the velocity vector of P_2 and the z axis is perpendicular to the orbital plane.

The three-body gravitational parameter called μ

$$\mu = \frac{m_2}{m_1 + m_2} \tag{5}$$

where m_1 is the mass of P_1, and m_2 is the mass of P_2. One non-dimensional Length Unit (LU) is equal to the distance between the two primaries, so the distance along the x axis from the origin to P_1 is $-\mu$ LU and from the origin to P_2 is $1 - \mu$ LU. The Time Unit (TU) is defined such that orbital period of P_2 with respect to P_1 is 2π TU. The equations of motion for the CRTBP are

$$\ddot{x} - 2\dot{y} = x - (1-\mu)\frac{x+\mu}{r_1^3} - \mu\frac{x+\mu-1}{r_2^3} \tag{6}$$

$$\ddot{y} + 2\dot{x} = (1 - \frac{1-\mu}{r_1^3} - \frac{\mu}{r_2^3})y \tag{7}$$

$$\ddot{z} = (\frac{\mu-1}{r_1^3} - \frac{\mu}{r_2^3})z \tag{8}$$

where

$$r_1 = \sqrt{(x+\mu)^2 + y^2 + z^2}$$

$$r_2 = \sqrt{(x+\mu-1)^2 + y^2 + z^2}$$

4. ORBIT DETERMINATION

The Extended Kalman Filter (EKF) is one of the most common methods used in real-time navigation, and it is adopted in this work: a reference of the topic can be found on [24]. The state vector being estimated consists of the position and velocity of each spacecraft. For two spacecraft, the state vector can be written as

$$\mathbf{X} = [x_1\ y_1\ z_1\ \dot{x}_1\ \dot{y}_1\ \dot{z}_1\ x_2\ y_2\ z_2\ \dot{x}_2\ \dot{y}_2\ \dot{z}_2]^T \tag{9}$$

where the subscripts denote the spacecraft number. The integration for the reference trajectory and the state transition matrix from t_{k-1} to t_k

$$\dot{\mathbf{X}}^* = \boldsymbol{F}(\mathbf{X}^*, t), \qquad \mathbf{X}^*(t_{k-1}) = \hat{\mathbf{X}}_{k-1} \tag{10}$$

the state transition matrix is obtained by integrating

$$\dot{\boldsymbol{\Phi}}(t, t_{k-1}) = \boldsymbol{A}(t)\boldsymbol{\Phi}(t, t_{k-1}) \tag{11}$$

with an initial condition $\boldsymbol{\Phi}(t_{k-1}, t_{k-1}) = \boldsymbol{I}$

$$\boldsymbol{A}(t) = \left[\frac{\partial \boldsymbol{F}(\boldsymbol{X}, t)}{\partial \boldsymbol{X}}\right]^* = \begin{bmatrix} \frac{\partial \dot{x}_1}{\partial x_1} & \frac{\partial \dot{x}_1}{\partial y_1} & \frac{\partial \dot{x}_1}{\partial z_1} & \cdots & \frac{\partial \dot{x}_1}{\partial \dot{z}_2} \\ \frac{\partial \dot{y}_1}{\partial x_1} & \frac{\partial \dot{y}_1}{\partial y_1} & \frac{\partial \dot{y}_1}{\partial z_1} & & \\ \frac{\partial \dot{z}_1}{\partial x_1} & \frac{\partial \dot{z}_1}{\partial y_1} & \frac{\partial \dot{z}_1}{\partial z_1} & & \vdots \\ \vdots & & & \ddots & \\ \frac{\partial \ddot{z}_2}{\partial x_1} & & \cdots & & \frac{\partial \ddot{z}_2}{\partial \dot{z}_2} \end{bmatrix}$$

and

$$\bar{\boldsymbol{P}}_k = \boldsymbol{\Phi}(t_k, t_{k-1})\boldsymbol{P}_{k-1}\boldsymbol{\Phi}^T(t_k, t_{k-1}) + \boldsymbol{Q} \tag{12}$$

$$\mathbf{y}_k = \mathbf{Y}_k - \boldsymbol{G}(\boldsymbol{X}_k^*, t_k) \tag{13}$$

where $\bar{\boldsymbol{P}}_k$ is the covariance matrix (time updated) at time t_k. State noise compensation is introduced by adding a matrix $\boldsymbol{Q}$, constructed as a 6x6 matrix for each spacecraft, to prevent filter saturation [4]. In this study, a constant $\boldsymbol{Q}$ is considered for each different scenario.

Regarding the measurement, pseudorange, involves the geometric range, the overall clock bias, and other error sources. In [25], the iterative solutions of two light time equations for the uplink and the downlink path are given. Basically, a two-way range measurement can be recorded by a mothercraft at time t, which has been received and transmitted by a daughtercraft at time $t - \tau_d$. Thus, the transmission time of the ranging signal by the mothercraft is given by $t - \tau_d - \tau_u$ where τ_d and τ_u are the downlink and the uplink light time respectively. The algorithm for the light-time solution is given by the following equations [25]:

$$\rho_d = c\tau_d^{i+1} = |\boldsymbol{r_2}(t - \tau_d^i) - \boldsymbol{r_1}(t)| \tag{14}$$

4

$$\rho_u = c\,\tau_u^{i+1} = |\mathbf{r_2}(t - \tau_d) - \mathbf{r_1}(t - \tau_d - \tau_u^i)| \qquad (15)$$

A fixed point iteration of Equation 14 and 15 is performed respectively until both τ_d and τ_u being better than a certain threshold. Then average value of the uplink range ρ_u and downlink range ρ_d give the two way range measurement [25].

Figure 5 presents the two-way ranging measurement process considered in this paper. During this measurement interval, both spacecraft are moved to their final relative position, $\mathbf{R}$, so there are changes in line-of-sight direction which can be modeled as $\Delta\rho$. In the end we can model the geometric range as

$$R = \frac{1}{2}\,c\,(t_3 - t_1) + \Delta\rho \qquad (16)$$

By assuming the speed of light is greater than the spacecraft relative velocity, $c \gg v$, we can model the geometric range as

$$R = \sqrt{(\mathbf{r_1} - \mathbf{r_2}) \cdot (\mathbf{r_1} - \mathbf{r_2})}$$
$$R = \sqrt{(x_1 - x_2)^2 + (y_1 - y_2)^2 + (z_1 - z_2)^2} \qquad (17)$$

Now, the pseudorange observations can be modeled as

$$\rho = R + c(\psi_{t_3} - \psi_{t_1}) + c\,(\Delta_{tx} + \Delta_{rx}) + c\,\Delta_{trx} + \rho_{\text{noise}}$$

$$\rho = \sqrt{(\mathbf{r_1} - \mathbf{r_2}) \cdot (\mathbf{r_1} - \mathbf{r_2})} + \rho_{\text{bias}} + \rho_{\text{noise}} \qquad (18)$$

where ψ_{t_4} and ψ_{t_1} are the clock states at t_4 and t_1 respectively. Δ_{tx} and Δ_{rx} are the transponder transmit and receive line delays respectively and Δ_{trx} is the line delay on the satellite B. All these terms are combined these terms as ρ_{bias} and ρ_{noise} represents the unmodelled error sources.

The observations can be related to the state with observation-state matrix

$$\tilde{\boldsymbol{H}}_k = \frac{\partial \boldsymbol{G}(\mathbf{X}_k^*, t_k)}{\partial \mathbf{X}_k} \qquad (19)$$
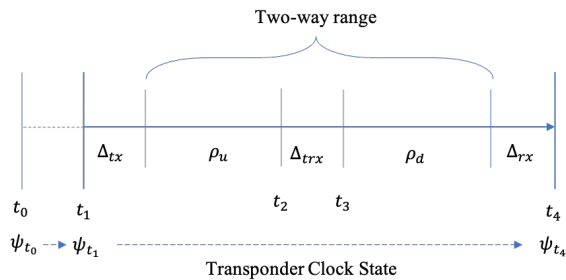

Figure 5. Two-way round-trip light time measurement.

In this study, the crosslink range ρ is the observation type, so $\tilde{\boldsymbol{H}}_k$ becomes

$$\tilde{\boldsymbol{H}}_k = \left[\frac{\partial\rho}{\partial x_1}\, \frac{\partial\rho}{\partial y_1}\, \frac{\partial\rho}{\partial z_1}\, \frac{\partial\rho}{\partial \dot{x}_1}\, \frac{\partial\rho}{\partial \dot{y}_1}\, \frac{\partial\rho}{\partial \dot{z}_1}\, \frac{\partial\rho}{\partial x_2}\, \frac{\partial\rho}{\partial y_2}\, \frac{\partial\rho}{\partial z_2}\, \frac{\partial\rho}{\partial \dot{x}_2}\, \frac{\partial\rho}{\partial \dot{y}_2}\, \frac{\partial\rho}{\partial \dot{z}_2} \right]_k \qquad (20)$$

If it is assumed that the observation errors can be modeled as white Gaussian noise with standard deviation σ_p, a weighting matrix $\boldsymbol{R}^{-1}$ can be used to weight observations as $R = \sigma_p^2$ and the Kalman gain matrix can be calculated

$$\boldsymbol{K}_k = \bar{\boldsymbol{P}}_k \tilde{\boldsymbol{H}}_k^T [\tilde{\boldsymbol{H}}_k \bar{\boldsymbol{P}}_k \tilde{\boldsymbol{H}}_k^T + \boldsymbol{R}_k]^{-1} \qquad (21)$$

Measurement and error covariance update

$$\hat{\mathbf{x}}_k = \boldsymbol{K}_k \mathbf{y}_k \qquad (22)$$

$$\boldsymbol{P}_k = [\boldsymbol{I} - \boldsymbol{K}_k \tilde{\boldsymbol{H}}_k] \bar{\boldsymbol{P}}_k \qquad (23)$$

$$\hat{\mathbf{X}}_k = \mathbf{X}_k^* + \hat{\mathbf{x}}_k \qquad (24)$$

Lastly, t_k becomes t_{k-1} and the process continues till the end of observations.

Observability

As explained in the previous section, the observations can be related to the state with a partial differential matrix $\tilde{\boldsymbol{H}}_k$ at time t_k, as given in Equation 19. The $\tilde{\boldsymbol{H}}_k$ matrix can be mapped to the initial Jacobian at epoch t_0 with the State Transition Matrix (STM) as

$$\boldsymbol{H}_k = \tilde{\boldsymbol{H}}_k \boldsymbol{\Phi}(t_k, t_0) \qquad (25)$$

Combining all observations into a vector as

$$\boldsymbol{H} = \begin{bmatrix} \boldsymbol{H}_1 \\ \vdots \\ \boldsymbol{H}_l \end{bmatrix} \qquad (26)$$

After weighting the observations with $W = 1/\sigma_\rho^2$, the information matrix can be written as

$$\boldsymbol{\Lambda} = \boldsymbol{H}^T \boldsymbol{W} \boldsymbol{H} = \sum_{k=1}^{l} \boldsymbol{H}_k^T \boldsymbol{W} \boldsymbol{H}_k \qquad (27)$$

The condition number $cond(\boldsymbol{\Lambda})$, which is the ratio of the largest singular value to the smallest one, provides an indication of the observability. Using the information matrix in Equation 27, the singular value decomposition can be performed as

5

$$\mathbf{\Lambda} = \mathbf{U}\mathbf{\Sigma}\mathbf{V}^T \qquad (28)$$

where $\mathbf{U}$ and $\mathbf{T}$ are unitary matrices and $\mathbf{\Sigma}$ is a matrix of singular values. It is also possible to check the degree of observability by calculating the singular values of the observability matrix [26]. The state with a largest singular value is the most observable state and it gives the most observable information. Similarly, the state with the smallest singular value is the least observable state in the system. By using $\mathbf{V}^T$, states corresponding to each singular value can be found: the largest number in the columns of $\mathbf{V}^T$ corresponding any singular value shows the related states. By looking at all the columns of $\mathbf{V}^T$, we can sort the states from the most observable one to the least observable one. In addition to the previous points, it is also possible to check the effectiveness of the observation at t_i alone on the position/velocity of a specific spacecraft. This can be done by taking the square root of the maximum eigenvalue of each $\mathbf{\Lambda}_k$ or 3×3 position/velocity component of $\mathbf{\Lambda}_i$, $(\sqrt{\max \operatorname{eig}(\mathbf{\Lambda}_{i(3\times3)})})$ [5]. This dynamic observability analysis will be an indicator for the tracking/telemetry window planning.

5. NAVIGATION SIMULATIONS

This section presents the simulations results firstly, orbit determination results are shown and, thereafter, the relation between measurement and orbit determination accuracy and finally the observability analysis is presented. The initial states used in the analysis for EML$_1$, and EML$_2$ are listed in the Table 1.

In total six different cases are simulated, which are based on three different relative geometries and two different ranging accuracies for each of them. True and estimated satellite trajectories are generated by using the ODE113 solver in Matlab. In this analysis, $150\,\mathrm{m}\,(1\sigma)$ and $300\,\mathrm{m}\,(1\sigma)$ the inter-satellite ranging errors are assumed, representing strong and worst case signal conditions respectively. These numbers are in the expected range considering the link analysis of small

Table 1. Initial states of Lagrange point orbiters.

Satellite ID		EML$_2$	EML$_1$
	x	1.1785868	0.8614062
	y	0.0	0.0
Initial	z	-0.0468605	0.03140426
Value	$\dot{x}$	0.0	0.0
(LU, LU/TU)	$\dot{y}$	-0.1673971	-0.1608423
	$\dot{z}$	0.0	0.0

Table 2. Link budget assumptions for an inter-satellite link.

Parameter	Uplink Value	Downlink Value
Mean distance	$60\,000\,\mathrm{km}$	$60\,000\,\mathrm{km}$
Frequency	$2200\,\mathrm{MHz}$	$2200\,\mathrm{MHz}$
Tx power	$3\,\mathrm{dBW}$	$3\,\mathrm{dBW}$
Tx lossses	$1\,\mathrm{dB}$	$1\,\mathrm{dB}$
Tx antenna gain	$25\,\mathrm{dBi}$	$9\,\mathrm{dBi}$
Data rate	$2000\,\mathrm{bps}$	$5000\,\mathrm{bps}$
Rx losses	$1\,\mathrm{dB}$	$1\,\mathrm{dB}$
Rx G/T	$-21\,\mathrm{dBK}$	$-1\,\mathrm{dBK}$
Link Margin	$3\,\mathrm{dB}$	$3\,\mathrm{dB}$

satellite missions in literature. In the LUMIO mission, for example, the spacecraft will be orbiting at the EML$_2$ and will have an inter-satellite link with a lunar orbiter (see [20] for further details). Based on the link budget analysis given in [27], the inter-satellite uplink and downlink data rates are expected to be $1000\,\mathrm{bps}$ and $4000\,\mathrm{bps}$ respectively. This would give us 1σ ranging error of around $680\,\mathrm{m}$ (based on Equation 4). Based on different assumptions for the inter-satellite link given in Table 2, a 1σ ranging error of $172\,\mathrm{m}$ would be possible, thanks to the higher uplink data rate.

No bias is further assumed for range measurements and the measurement interval is set to $187.5\,\mathrm{s}$ for 10 days of simulations. Because the time-derived ranging method is used, satellites can track each other without interruptions, which is further assumed for these simulations.

The initial covariance matrix is set to diagonal for each position and velocity component as $1\,\mathrm{km}$ and $1\,\mathrm{cm/s}$ respectively. The initial position and velocity in each component have an (1σ) error of $500\,\mathrm{m}$ and $1\,\mathrm{mm/s}$ for both satellites respectively. The estimated RMS error results are computed right after the initial epoch, also covering the high initial state errors. In the Monte-Carlo analysis, RMS error results after the first day are also given.

In the remaining part of this section, three separate formations are simulated: L$_1$ Halo - Lunar Orbiter, L$_2$ Halo - Lunar Orbiter, and L$_1$ Halo - L$_2$ Halo orbiters are simulated with high inter-satellite measurement errors.

L_2 Halo - Lunar Orbiter

In this scenario, one spacecraft is located in a halo orbit at EML$_2$ and the other spacecraft is in a lunar orbit. At the initial time, the distance between spacecraft is around $68\,000\,\mathrm{km}$.

It is known that LiAISON works well for halo orbiters in the vicinity of L$_1$, L$_2$, and lunar orbiters and this simulation covers the same scenario but considers high measurement errors. In the case of a $150\,\mathrm{m}$ ranging accuracy, the EKF converges for both spacecraft to the correct state, as shown in Figure 6, 7, and 8.
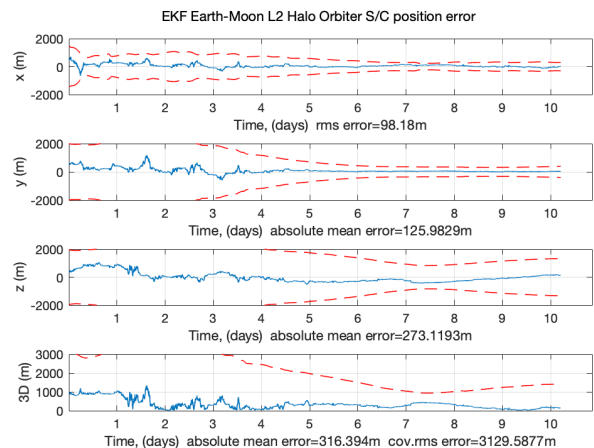

Figure 6. EML$_2$ Halo Orbiter position accuracy in the L$_2$ Halo - Lunar Orbiter with the $150\,\mathrm{m}$ ranging accuracy case.

Even with high initial uncertainties, the orbit estimates converged on three-dimensional $1\,\mathrm{km}$ position level after day-7 and day-1 for EML$_2$ halo orbiter and lunar orbiter re-

6

Figure 7. Lunar Orbiter position accuracy in the L_2 Halo - Lunar Orbiter with the 150 m ranging accuracy case.
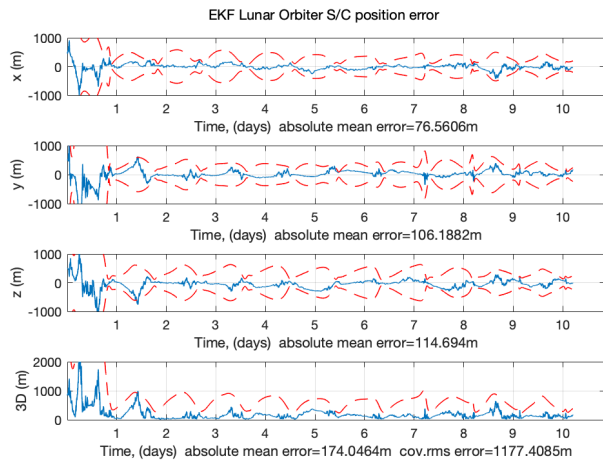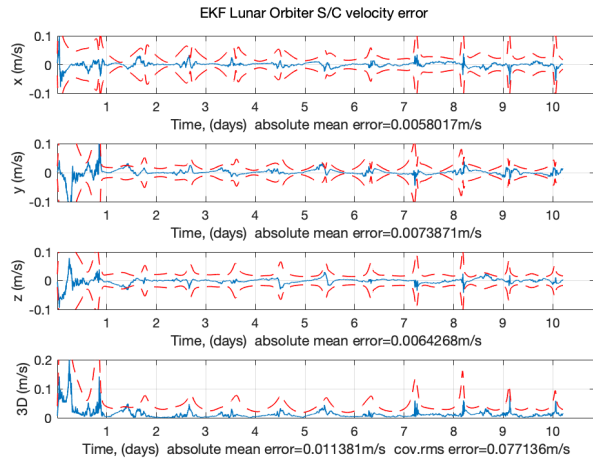

Figure 9. EML$_2$ Halo Orbiter position accuracy in the L_2 Halo - Lunar Orbiter with the 300 m ranging accuracy case.

Figure 8. Lunar Orbiter velocity accuracy in the L_2 Halo - Lunar Orbiter with the 150 m ranging accuracy case.
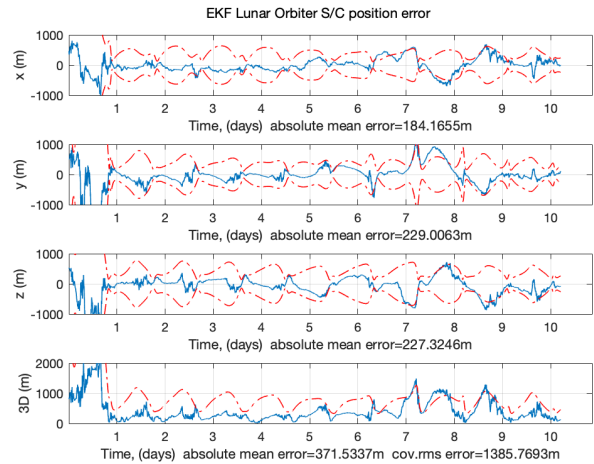
Figure 10. Lunar Orbiter position accuracy in the L_2 Halo - Lunar Orbiter with the 300 m ranging accuracy case.

spectively. This trend is also true for the velocity uncertainty. In the case of a 300 m ranging accuracy, estimated position/velocity accuracy and uncertainty are both almost doubled comparing to the 150 m case but still these are at an acceptable level (considering small satellites with an orbit determination requirement of less than 1 km position and 1 cm/s velocity), as can be seen in Figure 9 and 10. In addition to these, it can be said that estimated states are almost always in the 2-sigma bound over a 10-day span for both the 150 m and 300 m ranging accuracy cases.

The estimation errors give an absolute average position errors for the EML_2 halo orbiter of 316 m and 645 m RMS, velocity errors of 2.17 mm/s and 3.29 mm/s RMS, in the case of 150 m and 300 m ranging accuracy respectively. The absolute average position errors for the lunar orbiter is 174 m and 371 m RMS, with velocity errors of 11.38 mm/s and 25.73 mm/s RMS.
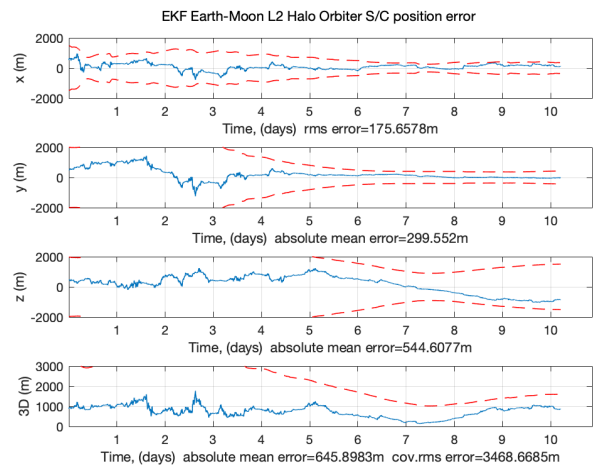
L_1 Halo - Lunar Orbiter

This scenario presents two spacecraft located in a halo orbit at EML$_1$ and in a lunar orbit. The initial distance between spacecraft is around 53 000 km. The same navigation results as in the L$_2$ Halo - Lunar Orbiter are observed for this scenario: the estimation trends for both 150 m and 300 m ranging accuracy are the same, as shown in Figures 11, 12, 13, and 14.

The estimation provides an absolute average position error for the EML_1 halo orbiter of 275 m and 662 m RMS, with velocity errors of 1.64 mm/s and 2.95 mm/s RMS, in case of 150 m and 300 m ranging accuracy cases respectively. The absolute average position errors for the lunar orbiter of 202 m and 423 m RMS, with velocity errors of 14.68 m/s and 29.35 m/s RMS, in case of 150 m and 300 m ranging accuracy cases respectively.

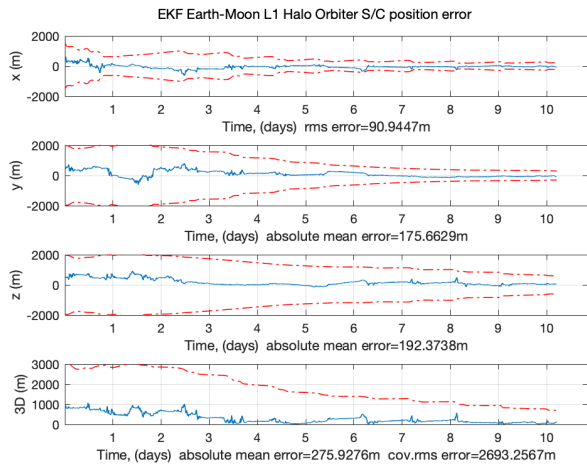Authorized licensed use limited to: TU Delft Library. Downloaded on August 17,2022 at 06:20:48 UTC from IEEE Xplore. Restrictions apply.

Figure 11. EML$_1$ Halo Orbiter position accuracy in the L$_1$ Halo - Lunar Orbiter with the $150\,\text{m}$ ranging accuracy case.
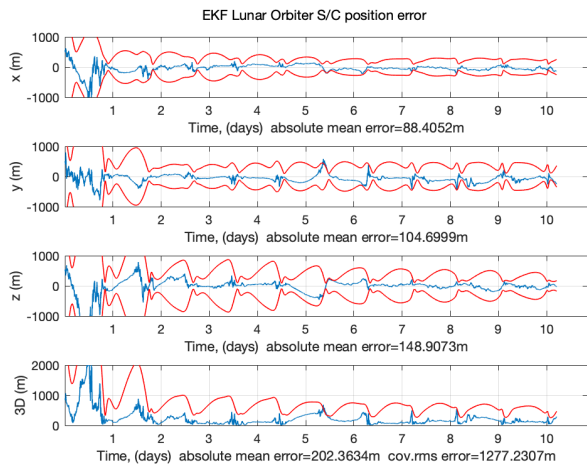
Figure 12. Lunar Orbiter position accuracy in the L$_1$ Halo - Lunar Orbiter with the $150\,\text{m}$ ranging accuracy case.

L$_1$ Halo - L$_2$ Halo Orbiter

This scenario presents two spacecraft located in halo orbits at EML$_1$ and EML$_2$. The initial distance between spacecraft is around $122\,000\,\text{km}$.

Regarding this scenario, the range measurements do not provide as much state information as lunar orbiter cases in terms of relative state changes. In the previous scenarios, the relative states change significantly at the same time, and range data provide all three dimensional position and velocity information even with high measurement errors. In other words, L$_1$ Halo - L$_2$ Halo case is less observable than the previous cases, so that it is affected more by high measurement errors. The estimated states for both satellites tend to diverge at certain geometries, which happened around day 7. In the end the RMS position and velocity errors for both satellites are higher than $2000\,\text{m}$ and $11.0\,\text{mm/s}$ respectively. Basically, if Doppler or range-rate observations had been used for this scenario, orbit determination results would have been improved.

Overall, all these scenarios are tested under 10 Monte Carlo runs and corresponding orbit determination results can be seen in Table 3. In Figure 15, the effect of the inter-satellite measurement error on the orbit determination error can be seen. In brief, these results show that a small satellite mission around EML$_1$ or EML$_2$, such as LUMIO, with an orbit determination requirement of less than $1\,\text{km}$ position and $1\,\text{cm/s}$ velocity would benefit from autonomous crosslink navigation with time-derived ranging in case there is an inter-satellite link with a Lunar orbiter. Basically, a mission designer may derive inter-satellite distance from the orbital geometry, then calculate the link budget to find out achievable data rates and directly expected ranging error. Thereafter, with the help of the results given in Figure 15, the expected orbit determination error can be derived and assesses against the mission requirements. These results are affected, as it can be expected, by measurement interval, relative geometry, orbital period, and other parameters.
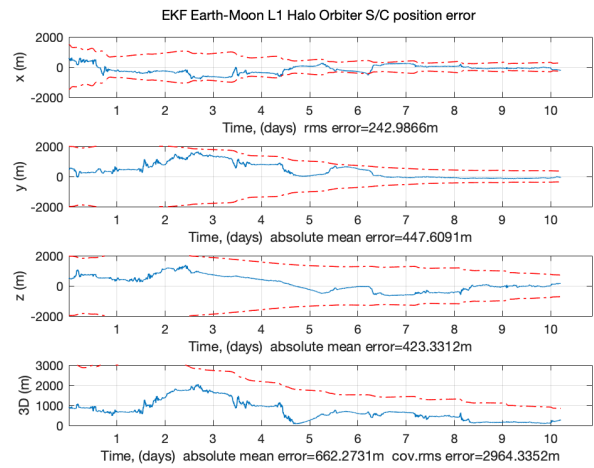

Figure 13. EML$_1$ Halo Orbiter position accuracy in the L$_1$ Halo - Lunar Orbiter with the $300\,\text{m}$ ranging accuracy case.
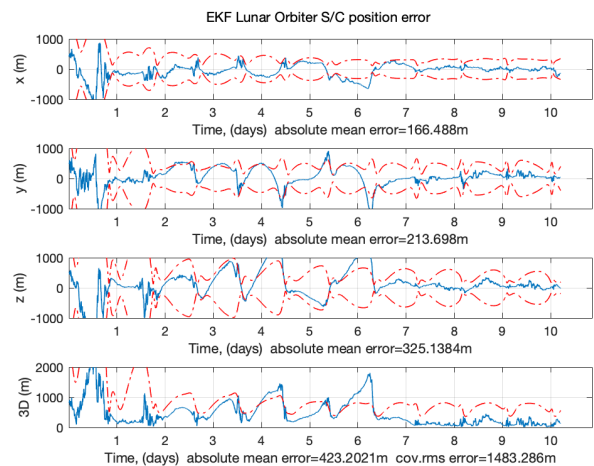

Figure 14. Lunar Orbiter position accuracy in the L$_1$ Halo - Lunar Orbiter with the $300\,\text{m}$ ranging accuracy case.

8

Table 3. Estimated position and velocity errors for three different scenarios with 10 Monte Carlo runs. RMS results after the first day are given in the brackets.

| Scenarios	S/C	Ranging Error (m)	Position Error (m) RMS	Velocity Error (m/s) RMS
EML$_2$-Lunar Orbiter	EML$_2$	150	434.44 [391.36]	0.00242 [0.00251]
	Lunar		196.30 [158.72]	0.01294 [0.01091]
	EML$_2$	300	734.29 [725.75]	0.00344 [0.00365]
	Lunar		337.28 [286.61]	0.02181 [0.01913]
EML$_1$-Lunar Orbiter	EML$_1$	150	408.53 [372.16]	0.00201 [0.00201]
	Lunar		238.56 [193.03]	0.01500 [0.01147]
	EML$_1$	300	558.79 [537.17]	0.00312 [0.00201]
	Lunar		389.24 [345.05]	0.02668 [0.02333]
EML$_1$-EML$_2$ Halo	EML$_1$	150	1717.78 [1830.28]	0.01277 [0.01386]
	EML$_2$		1938.93 [2159.82]	0.01067 [0.01161]
	EML$_1$	300	1846.57 [1969.11]	0.01393 [0.01517]
	EML$_2$		2054.60 [2059.82]	0.01350 [0.01241]
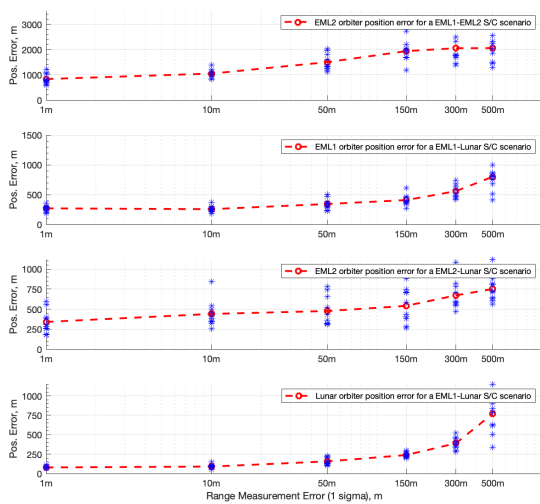
Figure 15. The effect of crosslink measurement error on orbit determination error for various scenarios

line-of-sight direction (axis of least positional uncertainty) so that observations do not provide any information about other directions. In Figure 16, the effectiveness of each observation on the position components of the Lunar orbiter can be seen. This also shows the similar results as in Figure 17.
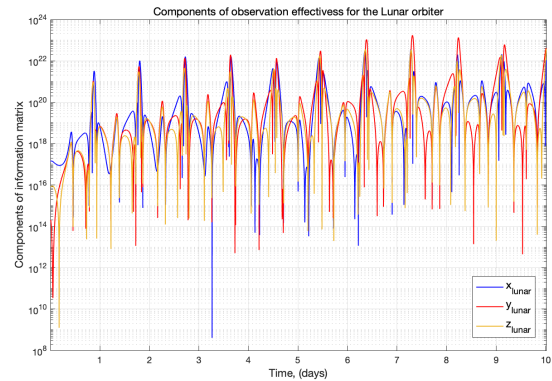

Figure 16. Components of observation effectiveness for the Lunar orbiter

Observability Analysis

This section presents the observation effectiveness for a EML$_2$-Lunar orbiters scenario. This dynamic observability analysis is done by calculating the information matrix, Equation 27 for all t_k, and then taking the square root of the maximum eigenvalue of each 3×3 position component of Λ_k for the EML$_2$ and Lunar orbiters. In Figure 17, the effectiveness of the observations for the EML$_2$ orbiter increases in time. On the other hand, the effectiveness fluctuates for the Lunar orbiter and multiple large jumps and dips are visible. During each dip period, observations do not provide any information, while valuable information is obtained during the peak intervals. The reason behind this fluctuation for the Lunar orbiter is related to the orbital geometry. When the Lunar orbiter approaches the periselene, the point in an orbit closest to the Moon, observations provide more valuable information in the measurement period due to the velocity of the spacecraft. The relative geometry changes significantly around this point, much more than at any other point in the orbit. In a similar way, the dip periods are related to the time around the aposelene, the point in an orbit farthest to the Moon, and related to the points in an orbit when the Lunar orbiter approaches the EML$_2$ orbiter on the

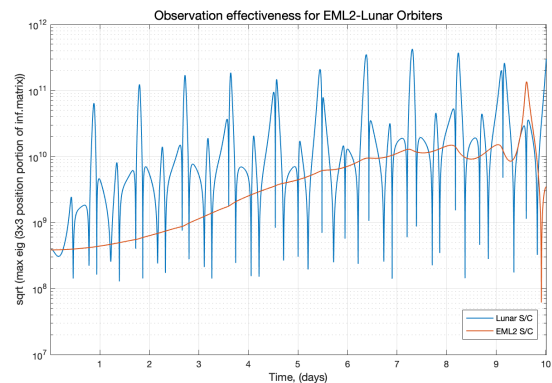**Figure 17**. Observation effectiveness for EML$_2$-Lunar Orbiters

As mentioned at the beginning, tracking sessions planning for orbit determination purposes coincides with telemetry sessions in case the time-derived or telemetry ranging methods are used for crosslink measurement purposes. This enables a flexible planning of the observations, scheduled in the peak observability points for best performances.

9

6. CONCLUSIONS

The aim of this study was to investigate the application of the LiAISON technique for multiple small spacecraft in cislunar orbits considering high inter-satellite range measurement errors due to data-aided ranging methods and without Doppler measurements. It was shown that the LiAISON autonomous orbit determination method is a useful method for cislunar orbiters even in case of a high inter-satellite measurement error. The simulation results showed that LiAISON navigation with high crosslink measurement errors estimates the true states of both spacecraft on the order of $100\,\mathrm{m}$ RMS error in case of EML_1, EML_2-Lunar orbiters, and on the order of $1000\,\mathrm{m}$ RMS error in case of EML_1, EML_2 orbiters. The results showed that a small satellite formation at EML_1 or EML_2 with orbit determination requirements less than $1\,\mathrm{km}$ (1σ) position and $1\,\mathrm{cm/s}$ (1σ) velocity would benefit from autonomous navigation using a link with a lunar orbiter. This study also showed that the time-derived and telemetry-based ranging methods can be an alternative to traditional ranging methods for an autonomous navigation architecture. The ranging accuracy depends on the achievable data rate, showing that high transmission power and high-gain antennas would be beneficial for such a small satellite formations.

In brief, the results presented in this study contribute to mature the design of satellite formations performing autonomous crosslink navigation, with special attention to small satellites and existing communication standards to obtain cost-effective solutions using existing hardware and protocols.

Future research could consider the potential effects of clock bias and drift on the navigation performance.

REFERENCES

[1] D. M. McIntosh, J. D. Baker, and J. A. Matus, "The nasa cubesat missions flying on artemis-1," 2020.

[2] K. Hill, J. Parker, G. Born, and N. Demandante, "A lunar l2 navigation, communication, and gravity mission," in *AIAA/AAS Astrodynamics Specialist Conference and Exhibit*. American Institute of Aeronautics and Astronautics, aug 2006.

[3] K. Hill and G. H. Born, "Autonomous interplanetary orbit determination using satellite-to-satellite tracking," *Journal of Guidance, Control, and Dynamics*, vol. 30, no. 3, pp. 679–686, may 2007.

[4] K. A. Hill and G. H. Born, "Autonomous orbit determination from lunar halo orbits using crosslink range," *Journal of Spacecraft and Rockets*, vol. 45, no. 3, pp. 548–553, may 2008.

[5] K. A.Hill, "Autonomous navigation in libration point orbits," Ph.D. dissertation, University of Colorado, 2007.

[6] S. Hesar, J. Parker, J. Mcmahon, and G. Born, "Small body gravity field estimation using liaison supplemented optical navigation," 01 2015.

[7] W. Wang, L. Shu, J. Liu, and Y. Gao, "Joint navigation performance of distant retrograde orbits and cislunar orbits via LiAISON considering dynamic and clock model errors," *Navigation*, vol. 66, no. 4, pp. 781–802, dec 2019.

[8] J. M. Leonard, "Supporting crewed missions using liaison navigation in the earth-moon system," Ph.D. dissertation, University of Colorado, 2015.

[9] K. Fujimoto, N. Stacey, and J. M. Turner, "Stereo-scopic image velocimetry as a measurement type for autonomous asteroid gravimetry," in *AIAA/AAS Astrodynamics Specialist Conference*. American Institute of Aeronautics and Astronautics, sep 2016.

[10] K. Fujimoto, J. Leonard, R. McGranaghan, J. Parker, R. Anderson, and G. Born, "Simulating the liaison navigation concept in a geo+ earth-moon halo constellation," 2012.

[11] N. Stacey and S. D'Amico, "(preprint) aas 18-448 autonomous swarming for simultaneous navigation and asteroid characterization," 2018.

[12] T. Gardner, B. Cheetham, A. Forsman, C. Meek, E. Kayser, J. Parker, M. Thompson, T. Latchu, R. Rogers, B. Bryant *et al.*, "Capstone: A cubesat pathfinder for the lunar gateway ecosystem," 2021.

[13] J. B. Berner, "Deep space network in the cubesat era," *IEEE Aerospace and Electronic Systems Magazine*, vol. 34, no. 4, pp. 46–54, 2019.

[14] J. Hamkins, P. Kinman, H. Xie, V. Vilnrotter, and S. Dolinar, "Telemetry ranging: Concepts," *IPNPR*, vol. 42, pp. 1–20, 2015.

[15] G. Iraci and C. Gnam, "An open source radio for low cost small satellite ranging," 08 2018.

[16] C. Foster, H. Hallam, and J. Mason, "Orbit determination and differential-drag control of planet labs cubesat constellations."

[17] K. Andrews, J. Hamkins, S. Shambayati, and V. Vilnrotter, "Telemetry-based ranging," in *2010 IEEE Aerospace Conference*. IEEE, 2010, pp. 1–16.

[18] CCSDS, "Pseudo-noise (pn) ranging systems," Feb. 2014. [Online]. Available: https://public.ccsds.org/Pubs/414x0g2.pdf

[19] S. W. Asmar and S. Matousek, "Mars cube one (MarCO) shifting the paradigm in relay deep space operation," in *SpaceOps 2016 Conference*. American Institute of Aeronautics and Astronautics, may 2016.

[20] S. Speretta, F. Topputo, J. Biggs, P. D. Lizia, M. Massari, K. Mani, D. D. Tos, S. Ceccherini, V. Franzese, A. Cervone, P. Sundaramoorthy, R. Noomen, S. Mestry, A. do Carmo Cipriano, A. Ivanov, D. Labate, L. Tommasi, A. Jochemsen, J. Gailis, R. Furfaro, V. Reddy, J. Vennekens, and R. Walker, "LUMIO: achieving autonomous operations for lunar exploration with a CubeSat," in *2018 SpaceOps Conference*. American Institute of Aeronautics and Astronautics, may 2018.

[21] CCSDS, "Proximity-1 space link protocol - physical layer ccsds 211.1-b-4," Tech. Rep., 2013. [Online]. Available: https://public.ccsds.org/Pubs/211x1b4e1.pdf

[22] S. Woo, J. Gao, and D. Mills, "Space network time distribution and synchronization protocol development for mars proximity link," in *SpaceOps 2010 Conference*. American Institute of Aeronautics and Astronautics, apr 2010.

[23] H. Peng, X. Bai, and S. Xu, "Continuation of periodic orbits in the sun-mercury elliptic restricted three-body problem," *Communications in Nonlinear Science and Numerical Simulation*, vol. 47, pp. 1–15, jun 2017.

[24] B. Schutz, B. Tapley, and G. H. Born, *Statistical orbit determination*. Elsevier, 2004.

[25] O. Montenbruck and E. Gill, *Satellite orbits: models, methods and applications*. Springer Science & Business Media, 2012.

[26] J. Yim, J. Crassidis, and J. Junkins, "Autonomous orbit navigation of interplanetary spacecraft," in *Astrodynamics Specialist Conference*. American Institute of Aeronautics and Astronautics, aug 2000.

[27] S. Speretta, A. Cervone, A. Menicucci, E. Turan, E. Bertels, B. Bosman, and F. Topputo, "Designing the radio link for a lunar cubesat: the lumio case," 2021.

BIOGRAPHY

__Erdem Turan__ received his BSc in Astronautical Engineering from the University of Turkish Aeronautical Association in Turkey. He received his MSc in Defense Technologies from Istanbul Technical University. During his MSc research, he studied on guidance and navigation algorithms. Erdem is now a PhD candidate at the Delft University of Technology in the Netherlands and is focusing on radio frequency based autonomous navigation for satellite formation flying in deep space.

__Stefano Speretta__ Stefano Speretta received his MSc and PhD from Politecnico di Torino in Italy. He currently works as an Assistant Professor at the Delft University of Technology in The Netherlands. He focuses on radio communications and autonomous radio-navigation for distributed space systems. With an industrial background, he was involved in multiple small satellite missions targeting Earth observation and deep space exploration.

__Eberhard Gill__ Eberhard Gill received a diploma in physics and holds a PhD in theoretical astrophysics of the Eberhard-Karls-University Tuebingen, Germany. He holds a Master of Space Systems Engineering of the Delft University of Technology. Since 2007, he holds the Chair of Space Systems Engineering at the Faculty of Aerospace Engineering of the Delft University of Technology. He is also the Director of TU Delft Space Institute. The research interests of Dr. Gill are miniaturized space systems, navigation, distributed space systems and Systems Engineering. Dr. Gill has authored or co-authored more than 250 journal articles and conference papers and four text books: Relativity and the Earth's Rotation (Springer 1990), Satellite Orbits (Springer 2000), Applied Space Systems Engineering (McGraw-Hill 2009) and Distributed Space Missions for Earth System Monitoring (Springer 2013).